Communication

Bottom-Up Synthesis of Porous NiMo Alloy for Hydrogen Evolution Reaction

Kailong Hu [1], Samuel Jeong [1], Mitsuru Wakisaka [2,3], Jun-ichi Fujita [1] and Yoshikazu Ito [1,2,*]

[1] Institute of Applied Physics, Graduate School of Pure and Applied Sciences, University of Tsukuba, Tsukuba, Ibaraki 305-8573, Japan

[2] PRESTO, Japan Science and Technology Agency, Saitama 332-0012, Japan

[3] Graduate School of Engineering, Toyama Prefectural University, 5180 Kurokawa, Imizu, Toyama 939-0398, Japan

* Correspondence: ito.yoshikazu.ga@u.tsukuba.ac.jp; Tel.: +81-29-853-5247

Abstract: Bottom-up synthesis of porous NiMo alloy reduced by $NiMoO_4$ nanofibers was systematically investigated to fabricate non-noble metal porous electrodes for hydrogen production. The different annealing temperatures of $NiMoO_4$ nanofibers under hydrogen atmosphere reveal that the 950 °C annealing temperature is a key to produce bicontinuous porous NiMo alloy without oxide phases. The porous NiMo alloy as cathodes in electrical water splitting demonstrates not only almost identical catalytic activity with commercial Pt/C in 1.0 M KOH solution, but also superb stability for 12 days at an electrode potential of −200 mV (v. s. RHE).

Keywords: nanoporous; NiMo; non-noble metal catalyst; hydrogen evolution

1. Introduction

Nanoporous metals are key materials for energy engineering fields because of outstanding conductivity, bi-continuous open porous structures with tunable porosity, large surface area, excellent catalytic activities and high mechanical strength [1, 2]. Recently, nanoporous non-precious metals has been focused as electrodes and catalysts such as supercapacitor [3, 4], Li-air battery [5, 6], fuel cell and water electrolysis [7, 8], showing great potentials as precious metal-free electrodes. The fabrication process of nanoporous metal employs a dealloying method [1] that the solid solution alloy of precious metal and non-precious metal was electrochemically corroded in acidic electrolytes. However, in this method, the alloy combinations in the dealloying method is very limited and the non-precious metal of Ni, Fe and Cu is usually the one to be removed from the alloy, forming precious metal-based nanoporous structures. Therefore, the desirable design of non-precious metal has been explored to expand their applications.

Nanoporous non-precious metal have been synthesized by bottom-up approaches such as nanoparticle-sintering [9, 10] and reduction of metal oxides [11, 12]. Especially, the reduction of metal oxide is a powerful method to prepare nanoporous non-precious metal. One of attractive porous metals is NiMo alloy which is known as one of the best hydrogen evolution electrode catalyst [13, 14] for cost-effective and highly efficient hydrogen production in water electrolysis. Although different kind of NiMo alloy porous morphologies were investigated as HER catalysts including Ni_4Mo [15], NiMo nanopowder [16], NiMo nanowire [17], the performances show the HER performance is not very enhanced due to the absence of bi-continuous and monolithic porous structures. Indeed, the Ni foam supported Ni_4Mo nanoparticles and the three-dimensional NiMo nanowires significantly improved their HER activities. This means that bi-continuous and monolithic 3D electrode catalysts bring high reaction kinetics. Therefore, NiMo alloy with bicontinuous open porous 3D structure can be a central electrode catalyst for electrical water splitting combined with renewable energy such as wind, water and solar energies to produce eco-friendly hydrogen production without any carbon emission.

46   In this study, we have systematically investigated porous NiMo alloy with different annealing
47 temperatures from 400°C to 950°C to understand the formation of porous structures by reduction
48 under hydrogen atmosphere. Moreover, the electrochemical performances of resulting porous NiMo
49 alloy samples were tested in 1 M KOH electrolyte with the comparison of the best catalyst of platinum
50 (Pt). The durability test in 1 M KOH electrolyte was further carried out by cyclic voltammetry and
51 chronoamperometry measurements.

52 **2. Materials and Methods**

53   **Preparation of NiMoO$_4$ nanofibers**. NiMoO$_4$ nanofibers, synthesized by a standard
54 hydrothermal method [18, 19], were used as precursors to obtain 3D porous NiMo alloy through a
55 reductive annealing system. 2.5 mmol NiCl$_2$·6H$_2$O (wako, 98% purity) and 2.5 mmol Na$_2$MoO$_4$·2H$_2$O
56 (wako, 99% purity) were dissolved in 30 ml deionized water, and then was transferred into a 50 ml
57 Teflon coated stainless autoclave, which was kept at 150°C for 12 h. After the autoclave cooling down
58 to room temperature, the as-prepared NiMoO$_4$ nanofibers were washed by deionized water several
59 times with a centrifuge, and kept in deionized water.
60   **Preparation of porous NiMo alloy**. The NiMoO$_4$ nanofiber solution was dropped on Cu sheets,
61 and dried naturally for one day. The dried NiMoO$_4$ (5.0 g) was put into the center of a quartz tube
62 (φ30×φ27×1000 mm) furnace. The NiMoO$_4$ was reduced at various temperatures from 400−950°C for
63 20 min under the mixed atmosphere of hydrogen (100 sccm) and argon (200 sccm) to reduce oxides
64 for porous structure formation. After the annealing, the resulting reduced samples were removed
65 from the Cu sheets for measurements.
66   **Imaging and spectroscopic characterization**. The morphology and microstructure of 3D NiMo
67 alloy were characterized by a scanning electron microscope (SEM, JEOL JSM-4300). The X-ray
68 diffraction (XRD) was carried out using a RIGAKU SmartLab 9MTP diffractometer with a 9.0 kW
69 rotating anode generator (Cu Kα1 radiation; λ = 1.5406 Å). The X-ray photoelectron spectroscopy
70 (XPS, AXIS ultra DLD, Shimazu) with Al Kα and X-ray monochromator was utilized for surface
71 chemical compositions analysis. The surface area of porous NiMo sample was measured by the
72 Brunauer–Emmett–Teller (BET) methods using a BELSORP-mini II (BEL. JAPAN. INC) at 77.0 K. The
73 sample was heated at 120°C under vacuum for 48 hours before the measurements.
74   **Electrochemical characterizations**. Hydrodynamic voltammetry for HER and electrochemical
75 impedance spectroscopy (EIS) were conducted using an electrochemical workstation (Biologic, VSP-
76 300) equipped with a rotation disk electrode (RDE, 5 mm diameter glassy carbon, HOKUTO DENKO
77 corp.). A graphite plate, an Ag/AgCl electrode (HOKUTO DENKO corp.) and the porous NiMo
78 samples (5 mg) dispersed on the glassy carbon served as the counter electrode, the reference electrode
79 and the working electrode, respectively. The porous NiMo samples and 10wt% Pt/C (Sigma-Ardrich)
80 were dispersed uniformly on the surface of the glassy carbon electrode using Nafion (wako, 5%
81 DE521 CS type) as a binder. The Ag/AgCl electrode was compared with a flesh Ag/AgCl electrode to
82 check the differences of potential before use. All potentials were calculated with respect to RHE using
83 the equation: E(RHE) = E(Ag/AgCl) + 0.0591 × pH + 0.1976. The cyclic voltammetry (CV)
84 measurements after several cycles were recorded from −250 mV to +100 mV (v.s. RHE) at a sweep
85 rate of 10 mV/s in 1 M KOH electrolyte (pH=13.9) deaerated with Ar (99.999%) with disk rotation
86 speed of 1600 rpm to remove generated hydrogen bubbles. The electrode potential in the
87 hydrodynamic voltammogram was automatically iR-compensated with the Ohmic resistance
88 measured at +200 mV (v.s. RHE). The EIS measurement was carried out at −200 mV (v.s. RHE) with
89 an amplitude of 50 mV. The durability of the electrodes was tested by potential cycling between −250
90 mV to +100 mV (v.s. RHE) at 10 mV/s. The electrolyte after 2000 CV cycle test was collected and
91 analyzed through ICP-OES (Thermo Fisher Scientific IRIS Advantage DUO) to determine the
92 leaching amount from NiMo catalyst.
93
94
95

96   **3. Results and Discussion**

97   The fabrication process of 3D porous NiMo alloy, illustrated in Figure 1., was divided into two
98   main procedures. Firstly, the $NiMoO_4$ nanofibers, the precursor of porous NiMo, were synthesized
99   through a standard hydrothermal method at 150°C for 12 hours. Secondly, the resulting $NiMoO_4$
100   nanofibers dropped on Cu sheets and inserted into a quartz tube furnace were annealed at 400-950°C
101   for 20 min under the mixed gases of hydrogen and argon to reduce the oxidized precursor. After the
102   furnace cooling down to room temperature, the annealed $NiMoO_4$ samples were peeled off from the
103   Cu sheets for characterizations and measurements. Moreover, the sheet area easily reached to 2 cm²
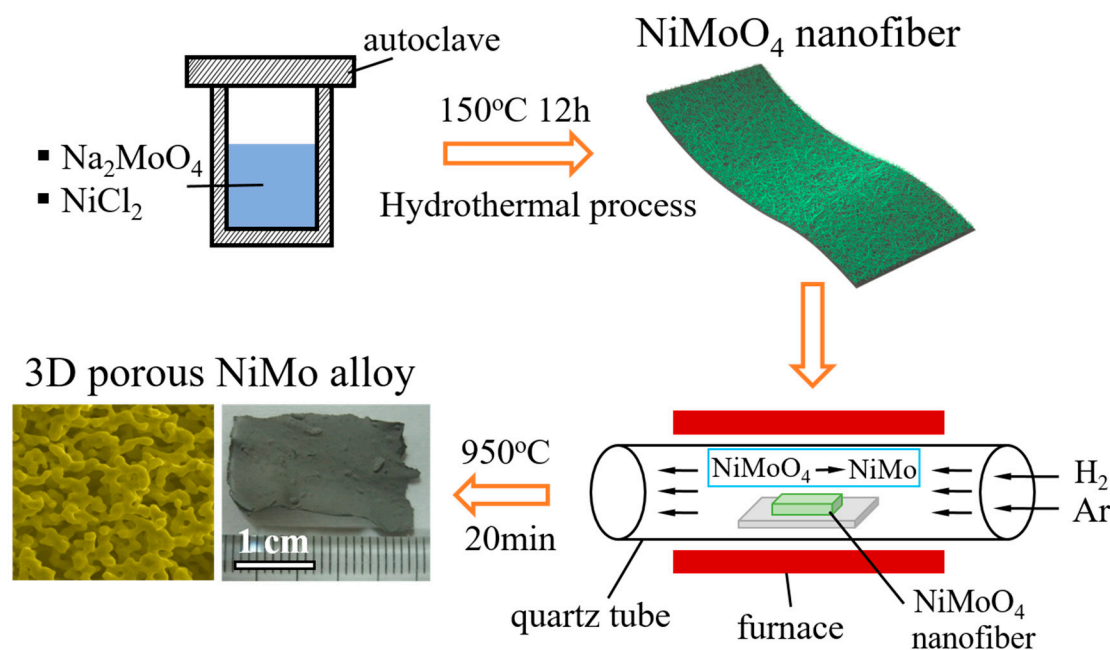104   (Figure 1) when the area of Cu sheet was tuned.

105

106   **Figure 1.** Schematic illustration of the synthesis process of 3D porous NiMo alloy.

107   The morphologies of annealed $NiMoO_4$ samples were investigated to reveal the formation
108   process of porous structures with scanning electron microscope (SEM) measurements. The nanofiber
109   structure was kept at low temperatures of 0-500°C (Figure 2a-c), and some nanoparticles were
110   generated on the surface of nanofibers at 500°C due to the reduction of $NiMoO_4$ nanofibers (inset of
111   Figure 2c). When the temperature reached to 600°C, the generated nanoparticles started to fuse and
112   reconstruct each other to be energetically stable due to the high geometric potential at the
113   nanoparticle state (Figure 2d). The pristine nanofiber structures were totally disappeared at 700°C
114   and the ligaments in the porous structures were gradually formed with pore size less than 100 nm
115   (Figure 2e). The 3D open porous structures were developed and the porous structures became
116   bicontinuous and interconnected above 800°C (Figure 2f). The porous structures were well developed
117   and the pore size increased from tens of nanometers to a few hundred nanometers with the
118   temperature ranging from 800 to 950°C (Figure 2g-h). The view of cross-section of sample annealed
119   at 950°C showed the open and bicontinuous structures were well preserved in the inside of sample
120   sheets (Figure 2i).
121   The crystal structures of annealed $NiMoO_4$ samples were studied by X-ray diffraction (XRD)
122   measurements (Figure 3a). The pristine $NiMoO_4$ nanofibers and sample annealed at 400°C matched
123   well with the $NiMoO_4 \cdot xH_2O$ (JCPDS #13-0128) (Figure S1). When the annealing temperature ranges
124   between 500-600°C, the obtained peaks were well assigned to $NiMoO_4$ (JCPDS #33-0948). This can be
125   explained with the complete removal of crystalline water at 500-600°C. At 700°C, some $NiMoO_4$ were
126   reduced and decomposed under the reductive atmosphere, partly forming NiO (JCPDS #71-1179)

127   and MoO_2 (JCPDS #65-5787). Above 800°C, the composition of NiMo (JCPDS #48-1745), Ni_4Mo
128   (JCPDS #65-5480), and pure Mo (JCPDS #42-1120) were gradually generated and oxidized species of
129   NiO and MoO_2 were gradually reduced. The $Ni(OH)_2$ (JCPDS #14-0117) was created from pure Ni
130   when it exposed into air for XRD measurements. It is worthy noted that the reduction of $NiMoO_4$
131   requires 800°C and reduction of MoO_2 requires 950°C. Thus, the sample annealed at 950°C only
132   obtains NiMo with certain amount of Ni_4Mo alloys. In addition, the high resolution XRD patterns of
133   samples annealed at 800°C, 900°C and 950°C are displayed in Figure S2. The specific surface area of
134   the porous NiMo annealed at 950°C was measured by the BET methods. The surface area was
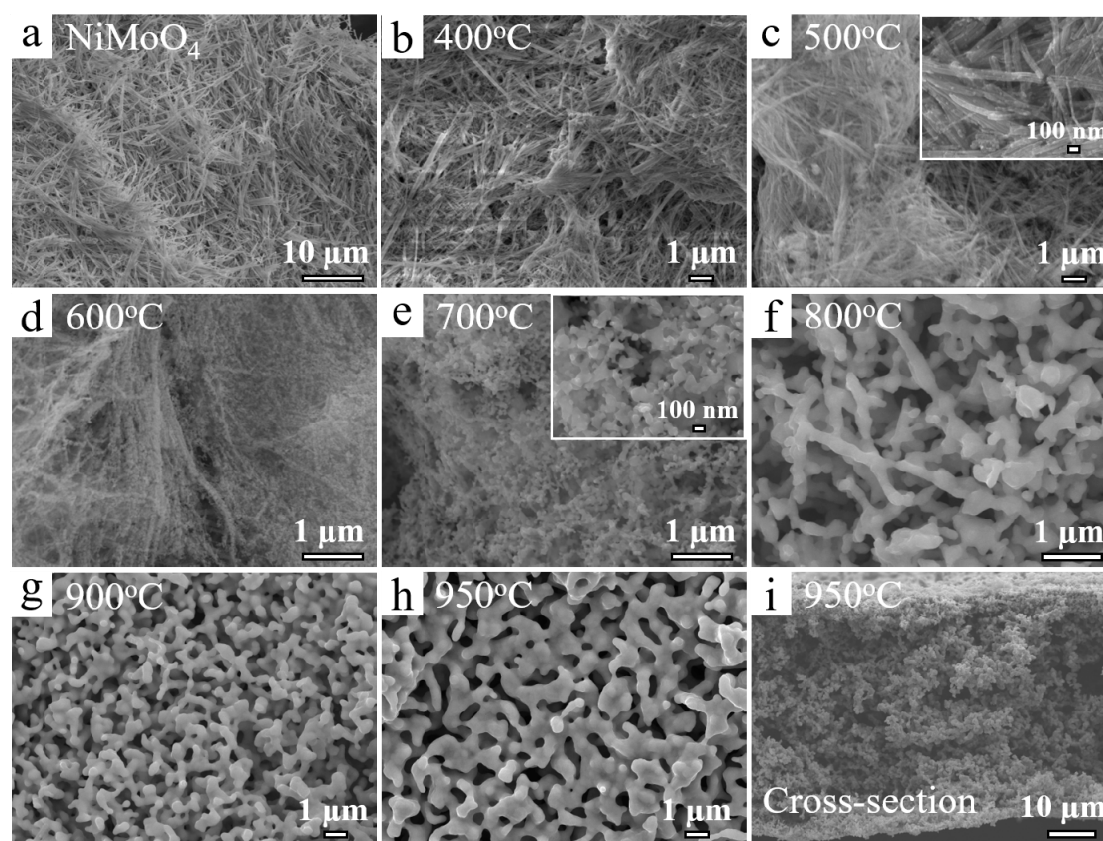135   estimated as 2.81 m^2/g (Figure S3).

136

Figure 2. SEM images of (**a**) pristine $NiMoO_4$ nanofiber; (**b-i**) temperature effect of 3D porous structure
formation on samples annealed at 400°C-950°C. The insets in (**c**) and (**e**) show high resolution SEM images.

139   The surface chemical compositions of porous NiMo and Ni_4Mo alloy samples annealed at 900°C
140   and 950°C were tested by X-ray photoelectron spectroscopy (XPS) measurements. The high-
141   resolution Ni 2p spectrum of the sample annealed at 900°C reveals that the main peaks are assigned
142   to Ni (852.6 eV, 869.6 eV) and NiO (855.9 eV, 873.6 eV), while the NiO peaks of the sample annealed
143   at 950°C are negligibly small (Figure 3b, 3d) [20-22]. These results further indicate that Ni oxides were
144   completely reduced at 950°C. The high-resolution Mo 3d spectrum of samples annealed at 900°C were
145   deconvoluted into six distinct peaks at 227.4 eV, 230.6 eV, 228.5 eV, 231.6 eV, 232.1 eV and 235.2 eV,
146   assigning to NiMo, Ni_4Mo and Mo oxide, showing alloy and oxidized surface state (Figure 3c) [23-
147   25]. The sample annealed at 950°C presents major NiMo (94.4 at%) with negligible Ni_4Mo (1.5 at%)
148   and Mo oxide on the surface, further confirming the almost complete reduction of Mo oxide (4.1 at%,
149   probably oxidized during the transfer to XPS measurements) at 950°C (Figure 3e). These XPS results
150   are good agreements with the XRD results. Considering XRD and XPS results during the reduction
151   process, the following sequential transformations are proposed: (1) the reduction of pristine $NiMoO_4$
152   to partly-reduced $NiMoO_4$ nanoparticles, (2) the reconstruction and fusion of the further-reduced
153    $NiMoO_4$ nanoparticles to decrease the surface energy and (3) the complete reduction of $NiMoO_4$

154   nanoparticles for the formation of ligaments into porous NiMo structures, developing 3D porous
155   NiMo alloy.
156   The samples with different annealing temperatures of 800ºC, 900ºC and 950ºC (abbreviated as
157   NiMo-800ºC, NiMo-900ºC and NiMo-950ºC) with the comparison of commercial 10wt% Pt/C and the
158   pristine $NiMoO_4$ nanofibers were tested in 1 M KOH solution to investigate the catalytic HER
159   activities (Figure 4a). The polarization curve of NiMo-950ºC exhibits a Pt-like HER activity, reaching
160   a current density of 10 mA/cm^2 at an overpotential of 18 mV, which is only 2 mV larger than the value
161   achieved by 10wt% Pt/C. Turnover frequency (TOF) normalized by the BET surface area at an
162   electrode potential of −100 mV (vs. RHE) was roughly estimated and the value was 0.84 H_2 s^{-1} for
163   NiMo-950ºC sample and the TOF value was relatively higher reported NiMo electrode (Table S1).
164   This means that the intrinsic catalyst activity of the NiMo-950ºC sample was enhanced by the bi-
165   continuous porous structures. The NiMo-900ºC and NiMo-800ºC reveal a gradual decline trend of
166   HER catalytic activity, which achieve 10 mA/cm^2 at an overpotential of 66 mV and 182 mV. This
167   decline indicates that the existence of Mo oxide and Ni oxide dramatically interferes HER processes,
168   and the HER activity can be greatly enhanced only with the complete reduction of the oxides at 950ºC.
169   Indeed, the fully oxidized $NiMoO_4$ nanofiber exhibits no HER catalytic activity. The Tafel plots
170   estimated from the polarization curves (Figure 4b) show that the NiMo-950ºC achieves a Tafel slope
171   of 36 mV/decade and 10wt% Pt/C (loading amount: 0.26 mg/cm^2) exhibits 30 mV/decade. Therefore,
172   the Heyrovsky desorption process (H_2O + e$^-$ + H* → H_2 + OH$^-$), where H* represents adsorbed H
173   atom on catalytic site *) could be the rate determining step for the NiMo-950ºC in 1 M KOH electrolyte
174   [26]. The Tafel slopes of NiMo-900ºC and NiMo-800ºC are 72 mV/dec and 147 mV/dec, indicating the
175   mixed Volmer-Heyrovsky process (H_2O + e$^-$ + H* → H_2 + OH$^-$ and H_2O + e$^-$ → H* + OH$^-$) are the
176   corresponding rate determining steps [27, 28]. The EIS measurements were further carried out to
177   measure the charge-transfer resistances (R_{ct}) of the porous NiMo alloys at an overpotential of 200 mV
178   v.s. RHE (Figure 4c). The internal resistances of NiMo-800ºC, NiMo-900ºC and NiMo-950ºC are
179   almost the same value of 5 Ω. The NiMo-950ºC exhibits quite low R_{ct} value of 7.9 Ω, which far lower
180   than the 19.8 Ω for NiMo-900ºC and the 26.5 Ω for NiMo-800ºC, confirming more efficient reaction
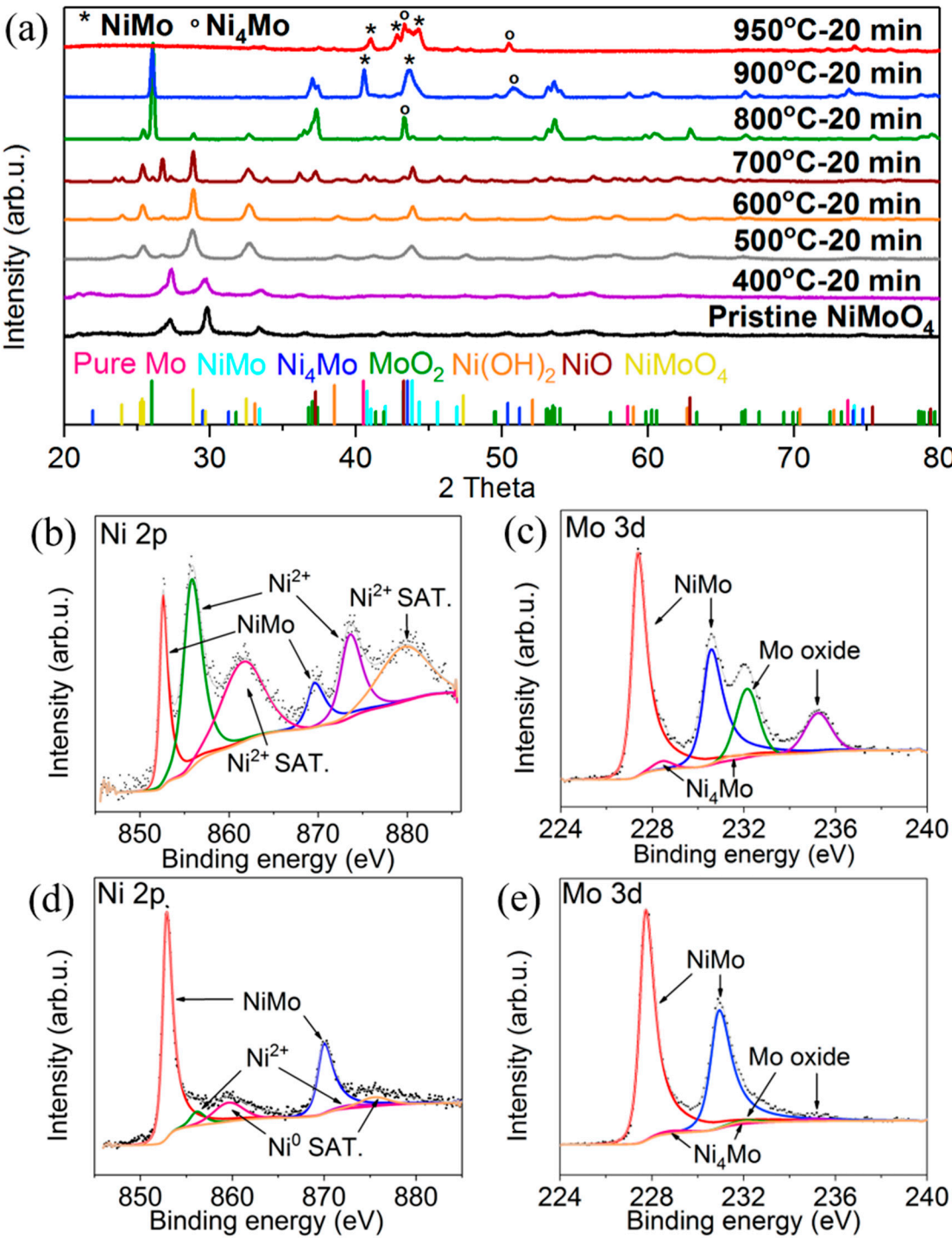181   kinetics of the NiMo-950ºC sample. All electrochemical properties were listed in Table S1.

Figure 3. (**a**) XRD patterns of pristine NiMoO$_4$ nanofibers and reduced samples at different annealing temperatures. High-resolution XPS spectra of nickel 2p and molybdenum 3d spectra on porous NiMo samples annealed at 900°C for 20 min; (**b–c**) and 950°C for 20 min (**d–e**).
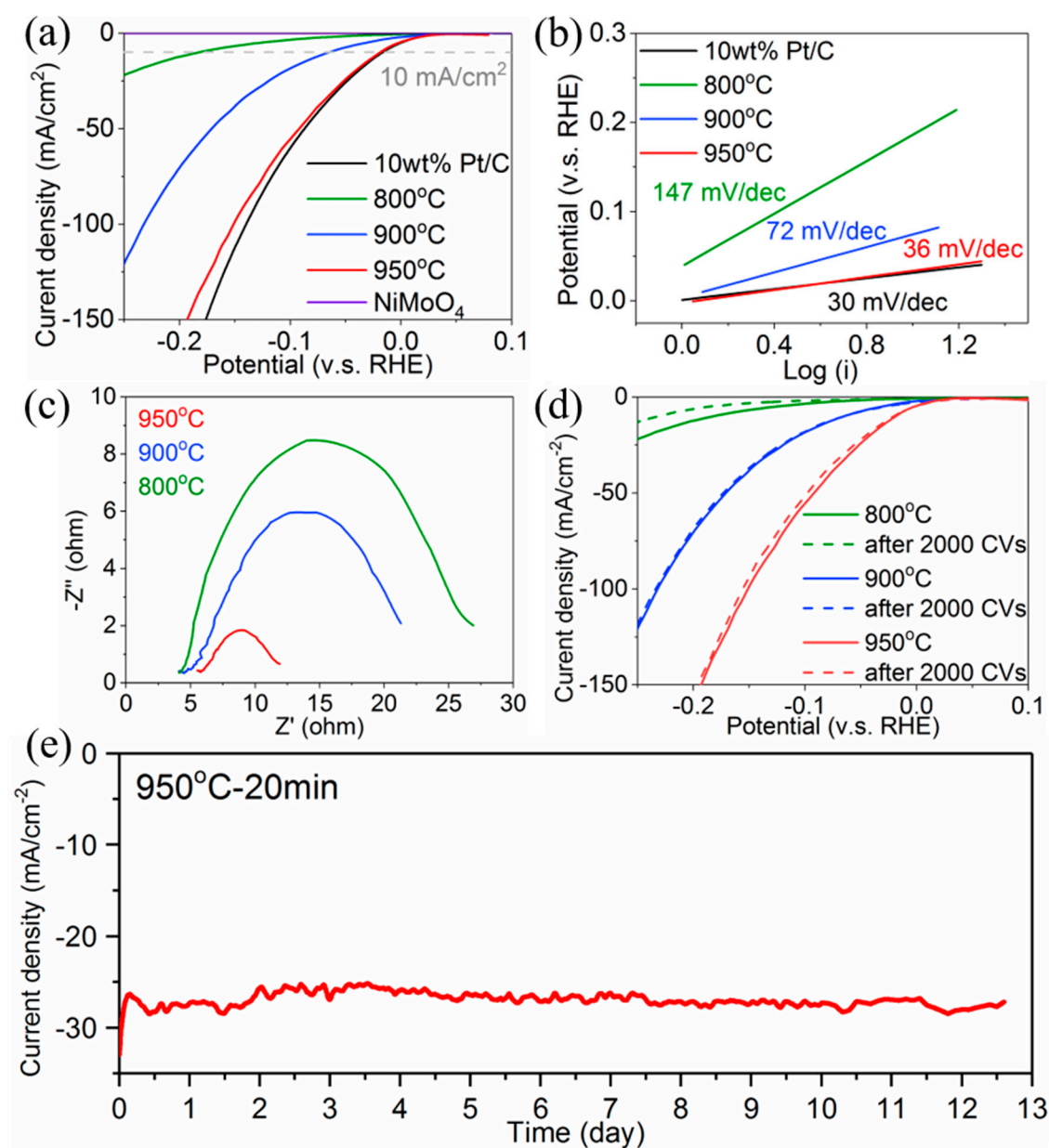
186

Figure 4. (**a**) The HER polarization curves of porous NiMo samples annealed at 800°C, 900°C, 950°C, pristine NiMoO₄ nanofibers and 10wt% Pt/C. (**b**) Corresponding Tafel plots from (a). (**c**) Electrochemical impedance spectroscopy of porous NiMo samples annealed at 800°C, 900°C and 950°C at overpotential of 200 mV v.s. RHE. (**d**) Polarization curves of porous NiMo samples annealed at 800°C, 900°C and 950°C before and after 2000 CV cycles. (**e**) Durability test of porous NiMo annealed at 950°C at overpotential of 200 mV by chronoamperometry.
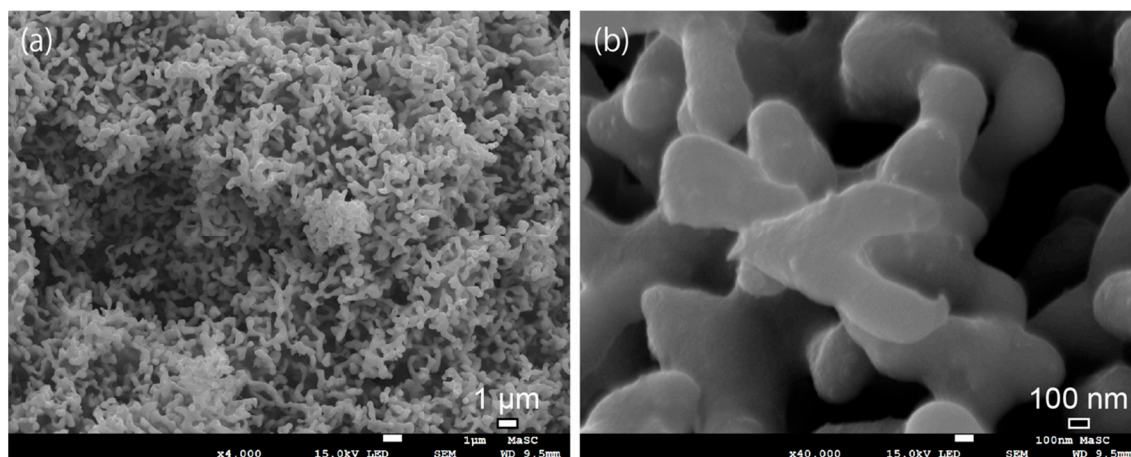
Figure 5. SEM images of porous NiMo samples annealed at 950°C after 2000 CV cycles.

The long-term durability is an important criterion for HER cathodes. The CV and chronoamperometry (CA) measurements were utilized to investigate the stability of porous NiMo alloy at an electrode potential of −200 mV (vs. RHE) in 1 M KOH electrolyte. The polarization curves of NiMo-900°C and NiMo-950°C after 2000 cycles exhibit extremely high durability (Figure 4d). The overpotential of NiMo-950°C at 100 mA/cm^2 only increases by 5 mV (150 to 155 mV) after the 2000 CV cycles. During the CA measurement (Figure 4e), the NiMo-950°C sample (loading amount: 1 mg) keeps original performances of 27 mA/cm^2 for 12.5 days at overpotential of 200 mV. A rotating disk electrode was not used for the CA test, resulting in some bubbles blocked the surface and a slight decrease of the current density. To understand the superb HER performances and chemical stability, the SEM images of the NiMo-950°C sample after 2000 CV cycles were investigated. The bicontinuous porous structure was well preserved in 1 M KOH electrolyte (Figure 5). In addition, the ICP-OES was used to investigate the leaching amount of the NiMo electrode after 2000 cycle test. The result reveal that the dissolution amount of Ni and Mo is less than 0.6 at% and 0.3 at% (under the detection limit), which further confirm the prominent stability. Thus, chemically stable and well-crystalized porous NiMo-950°C alloy electrode plays an important role of outstanding HER performances.

4. Conclusions

We have demonstrated the formation of porous NiMo alloy with systematic annealing temperatures from 400-950°C. The formation of porous structures requires 800°C, and the complete reduction of Mo oxide species requires 950°C annealing temperature. The bi-continuous and conductive porous NiMo alloys with larger surface area can enhance intrinsic catalyst activity and would be employed as cathodes for electrical water splitting without losing their catalytic abilities in 1 M KOH electrolyte for 12.5 days. Such non-noble porous metal alloys could be good replacements of noble metal such as Pt, which has been one of undue barrier to sustaining worldwide use due to high price and low world supply. Therefore, the development and study of non-noble porous metals as low-cost, earth-abundant HER catalysts offer hopeful alternatives to Pt-based catalysts to achieve hydrogen societies.

Author Contributions: Hu Kailong, Samuel Jeong and Yoshikazu Ito fabricated samples and conducted SEM characterizations. Yoshikazu Ito and Hu Kailong performed electrochemical tests. Hu Kailong, Mitsuru Wakisaka, Jun-ichi Fujita and Yoshikazu Ito conducted data analysis and data interpretation. Hu Kailong and Yoshikazu Ito wrote the paper.

230   **Conflicts of Interest:** The authors declare no conflict of interest.

231   **References**

232   1.   Ding, Y.; Chen, M.W. Nanoporous metals for catalytic and optical applications. *MRS Bull.* 2009, 34, 569-
233   576.
234   2.   Weissmüller, J.; Newman, R.C.; Jin, H.J.; Hodge, A.M.; Kysar, J.W. Nanoporous metals by alloy corrosion:
235   formation and mechanical properties. *MRS Bull.* 2009, 34, 577-586.
236   3.   Qiu, H.J.; Ito, Y.; Chen, M.W. Hierarchical nanoporous nickel alloy as three-dimensional electrodes for
237   high-efficiency energy storage. *Scripta Materialia* 2014, 89, 69-72.
238   4.   Qiu, H.J.; Kang, J.L.; Liu, P.; Hirata, A.; Fujita, T.; Chen, M.W. Fabrication of large-scale nanoporous nickel
239   with a tunable pore size for energy storage. *J. Power Sources* 2014, 247, 896-905.
240   5.   Guo, X.W.; Han, J.H.; Liu, P.; Ito, Y.; Hirata, A.; Chen, M.W. Graphene@Nanoporous Nickel Cathode for
241   Li-O$_2$ Batteries. *ChemNanoMat* 2016, 2, 176-181.
242   6.   Guo, X.W.; Liu, P.; Han, J.H.; Ito, Y.; Hirata, A.; Fujita, T.; Chen, M.W. 3D Nanoporous Nitrogen-Doped
243   Graphene with Encapsulated RuO$_2$ Nanoparticles for Li-O$_2$ Batteries. *Adv. Mater.* 2015, 27, 6137-6143.
244   7.   Linic, S.; Christopher, P.; Ingram, D.B. Plasmonic-metal nanostructures for efficient conversion of solar to
245   chemical energy. *Nature Mater.* 2011, 10, 911-921.
246   8.   Artero, V.; Kerlidou, M.C.; Fontecave, M. Splitting Water with Cobalt. *Angew. Chem. Int. Ed. Engl.* 2011, 50,
247   7238-7266.
248   9.   Ito, Y.; Izumi, M.; Hojo, D.; Wakisaka, M.; Aida, T.; Adschiri, T. One-step Nanoporous Structure Formation
249   Using NiO Nanoparticles: Pore Size Control and Pore Size Dependence of Hydrogen Evolution Reaction.
250   *Chem. Lett.* 2017, 46, 267-270.
251   10.   Hansen, T.W.; DeLaRiva, A.T.; Challa, S.R.; Datye, A.K. Sintering of Catalytic Nanoparticles: Particle
252   Migration or Ostwald Ripening? *Acc. Chem. Res.* 2013, 46, 1720-1730.
253   11.   Zhang, J.; Wang, T.; Liu, P.; Liao, Z.Q.; Liu, S.H.; Zhuang, X.D.; Chen, M.W.; Zschech, E.; Feng, X.L. Efficient
254   hydrogen production on MoNi$_4$ electrocatalysts with fast water dissociation kinetics. *Nat. Commun.* 2017,
255   8, 15437.
256   12.   Chen, Y.Y.; Zhang, Y.; Zhang, X.; Tang, T.; Luo, H.; Niu, S.; Dai, Z.H.; Wan, L.J.; Hu, J.S. Self-Templated
257   Fabrication of MoNi$_4$/MoO$_{3-x}$ Nanorod Arrays with Dual Active Components for Highly Efficient
258   Hydrogen Evolution. *Adv. Mater.* 2017, 1703311.
259   13.   McCrory, C.C.; Jung, S.; Ferrer, I.M.; Chatman, S.M.; Peters, J.C.; Jaramillo, T.F. Benchmarking hydrogen
260   evolving reaction and oxygen evolving reaction electrocatalysts for solar water splitting devices. *J. Am.*
261   *Chem. Soc.* 2015, 137, 4347-4357.
262   14.   McCrory, C.C.; Jung, S.; Peters, J.C.; Jaramillo, T.F. Benchmarking heterogeneous electrocatalysts for the
263   oxygen evolution reaction. *J. Am. Chem. Soc.* 2013, 135, 16977-16987.
264   15.   Jin, Y.S.; Yue, X.; Shu, C.; Huang, S.L.; Shen, P.K. Three-dimensional porous MoNi4 networks constructed
265   by nanosheets as bifunctional electrocatalysts for overall water splitting. *J. Mater. Chem. A* 2017, 5, 2508-
266   2513.
267   16.   McKone, J.R.; Sadtler, B.F.; Werlang, C.L.; Lewis, N.S.; Gray, H.B. Ni–Mo Nanopowders for Efficient
268   Electrochemical Hydrogen Evolution. *ACS Catal.* 2013, 3, 166–169.
269   17.   Fang, M.; Guo, W.; Dong, G.F.; Xia, Z.M.; Yip, S.P.; Qin, Y.B.; Qu, Y.Q.; Ho, J.C. Hierarchical NiMo-based
270   3D electrocatalysts for highly-efficient hydrogen evolution in alkaline conditions. *Nano Energy* 2016, 27,
271   247-254.
272   18.   Jothi, P.R.; Kannan, S.; Velayutham, G. Enhanced methanol electro-oxidation over in-situ carbon and
273   graphene supported one dimensional NiMoO4 nanorods. *J. Power Sources* 2015, 277, 350-359.
274   19.   Kuang, P.Y.; Tong, T.; Fan, K.; Yu, J.G. In Situ Fabrication of Ni–Mo Bimetal Sulfide Hybrid as an Efficient
275   Electrocatalyst for Hydrogen Evolution over a Wide pH Range. *ACS Catal.* 2017, 7, 6179–6187.
276   20.   G. K. Wertheim; J. H. Wernick; G. Crecelius. Surface effects on valence in rare-earth intermetallic
277   compounds. *Phys. Rev. B* 18, 875.
278   21.   A. Roustila; C. Severac; J. Chêne; A. Percheron-Guégan. Hydrogen effects on the electronic and
279   microstructural properties of Ce, Ni, and CeNi2 intermetallic compound. *Surface Science* 1994, 311, 33-44.
280   22.   A. Lebugle; U. Axelsson; R. Nyholm; N. Mårtensson. Experimental L and M core level binding energies for
281   the metals 22Ti to 30Zn. *Physica Scripta* 1981, 23, 825-827.

23. William A. Brainard; Donald R. Wheeler. An XPS study of the adherence of refractory carbide silicide and boride rf-sputtered wear-resistant coatings. *Journal of Vacuum Science & Technology* 1978, 15, 1800-1805.

24. C.L. Bianchi; M.G. Cattania; P. Villa. XPS characterization of Ni and Mo oxides before and after "in situ" treatments. Applied Surface Science 1993, 70, 211-216.

25. I. Takano; S. Isobe; T.A. Sasaki; Y. Baba. Nitrogenation of various transition metals by N+ 2-ion implantation. Applied Surface Science 1989, 37, 25-32.

26. Conway, B.E.; Tilak, B.V. Interfacial processes involving electrocatalytic evolution and oxidation of H_2, and the role of chemisorbed H. *Electrochim Acta* 2002, 47, 3571-3594.

27. Zheng, Y.; Jiao, Y.; Zhu, Y.H.; Li, L.H.; Han, Y.; Chen, Y.; Du, A.J.; Jaroniec, M.; Qiao, S.Z. Hydrogen evolution by a metal-free electrocatalyst. *Nat. Commun.* 2014, 5, 3783.

28. Liang, Z.X.; Ahn, H.S.; Bard, A.J. A Study of the Mechanism of the Hydrogen Evolution Reaction on Nickel by Surface Interrogation Scanning Electrochemical Microscopy. *J. Am. Chem. Soc.* 2017, 139, 4854–4858.